

# The 2.3 GHz continuum survey of the GEM project

C. Tello<sup>1</sup>, T. Villela<sup>1</sup>, S. Torres<sup>2</sup>, M. Bersanelli<sup>3</sup>, G. F. Smoot<sup>4,5</sup>, I. S. Ferreira<sup>1</sup>, A. Cingoz<sup>5</sup>, J. Lamb<sup>6</sup>, D. Barbosa<sup>7,8</sup>, D. Perez-Becker<sup>5,9</sup>, S. Ricciardi<sup>4,10</sup>, J. A. Curri van<sup>5</sup>, P. Platania<sup>11</sup>, and D. Maino<sup>3</sup>

<sup>1</sup> Divisão de Astrofísica, Instituto Nacional de Pesquisas Espaciais (INPE), CP 515, 12201-970, São José dos Campos, SP, Brazil

<sup>2</sup> Centro Internacional de Física, Bogotá, Colombia

<sup>3</sup> Dipartimento di Fisica, Università degli Studi di Milano, via Celoria 16, 20133 Milano, Italy

<sup>4</sup> Lawrence Berkeley National Laboratory, University of California, 1 Cyclotron Road, Bldg. 50, MS 205, Berkeley, CA 94720, USA

<sup>5</sup> Physics Department, University of California, Berkeley CA 94720, USA

<sup>6</sup> Physics Department, University of California, Santa Barbara CA 93106, USA

<sup>7</sup> Centro Multidisciplinar em Astrofísica, Instituto Superior Técnico, Av. Rovisco Pais, Lisboa, Portugal

<sup>8</sup> Grupo de RadioAstronomia, Instituto de Telecomunicações, Campus Universitário de Aveiro, Aveiro, Portugal

<sup>9</sup> Departamento de Física, Facultad de Ciencias, Universidad Nacional Autónoma de México, 04510 DF, Mexico

<sup>10</sup> INAF Osservatorio Astronomico di Padova, Vicolo dell'Osservatorio 5, I - 35122, Padova, Italy

<sup>11</sup> Istituto di Fisica del Plasma, CNR-ENEA-EURATOM Association, Via R. Cozzi 53, 20125 Milano, Italy

Received ; accepted

## ABSTRACT

**Context.** Determining the spectral and spatial characteristics of the radio continuum of our Galaxy is an experimentally challenging endeavour for improving our understanding of the astrophysics of the interstellar medium. This knowledge has also become of paramount significance for cosmology, since Galactic emission is the main source of astrophysical contamination in measurements of the Cosmic Microwave Background radiation.

**Aims.** In this paper we present the scope of the Galactic Emission Mapping (GEM) project and its results at 2.3 GHz. Its observational program was conceived and developed to reveal the large scale properties of Galactic synchrotron radiation in total intensity and polarisation through a self-consistent set of radio continuum surveys between 408 MHz and 10 GHz. GEM's unique observational strategy and experimental design aim at the production of foreground templates in order to address the mutual inconsistencies between existing surveys.

**Methods.** The GEM experiment uses a portable and double-shielded 5.5-m radiotelescope on a rotating platform to map 60° wide declination bands, from different observational sites, by circularly scanning the sky at 30° from the Zenith. The observations at 2.3 GHz were accomplished with a total power receiver, whose front-end HEMT was matched directly to a cylindrical horn at the prime focus of a parabolic reflector. The Moon was used to calibrate the antenna temperature scale and the preparation of the map required direct subtraction and destripping algorithms to remove ground contamination as the most significant source of systematic error.

**Results.** For this first GEM survey, 484 hours of observations were used from two locations in Colombia and Brazil to yield a 69% sky coverage from  $\delta = -53^\circ$  to  $\delta = +35^\circ$  with a horizontal HPBW of  $2.30^\circ$  and a vertical HPBW  $1.85^\circ$ . The pointing accuracy was  $8.6''$  and the RMS sensitivity was  $9.8 \pm 1.6$  mK. The zero-level uncertainty is 103 mK with a temperature scale error of 5% after direct correlation with the Rhodes/HartRAO survey at 2326 MHz on a  $T-T$  plot.

**Key words.** surveys – Galaxy: structure – radio continuum: general – radio continuum: ISM

## 1. Introduction

The large scale distribution of non-thermal radiation from our Galaxy has been observed since the birth of radioastronomy at very low frequencies of a few tenths of MHz (Jansky 1932; 1933; 1935) until the present era of precision cosmology (e.g. Mather et al. 1990; Smoot et al. 1992; de Bernardis et al. 2000; Bennett et al. 2003; Meinhold et al. 2005) at frequencies above 20 GHz. By the time its synchrotron nature was recognized to be due to relativistic electrons spiralling along interstellar magnetic field lines (Kiepenhauer 1950; Mayer et al. 1957; Mills 1959; Westerhout 1962; Wielebinski et al. 1962), another Galactic emission component (free-free radiation from HII regions) had already been identified through the pioneering work of Reber (1940), who sketched the first radio maps of the Galaxy at 160 MHz and 480 MHz (Reber 1935; Reber

1935). Excluding atmospheric emission and the 3 K Cosmic Microwave Background (CMB) radiation, the sky signal is dominated by synchrotron radiation up to  $\sim 25$  GHz and by free-free up to  $\sim 75$  GHz, where the rising spectrum of thermal dust takes over the characterization of Galactic emission all the way into the infra-red. Given this association with distinct astrophysical sources, each Galactic emission component traces a unique spatial template. In the case of the non-thermal continuum, radioastronomers have always been actively pursuing the frequency dependence of the synchrotron template in order to understand the structure and composition of the interstellar medium. In cosmology, the nature of temperature anisotropies in the CMB and its polarisation cannot be fully understood unless the contaminating role played by Galactic emission is clearly determined.

In this article, we present the first survey of an observational program, the Galactic Emission Mapping (GEM) project, aimed to supplement the frequency gap in the surveys of the ra-

dio continuum at centimeter wavelengths and the satellite maps from the *COBE* and *WMAP* missions in the millimetric band. We explore this connection in Sect. 2 and state our need to prepare a mutually consistent set of spatial templates of the synchrotron component between 408 MHz and 10 GHz, in total intensity and polarisation, as we overview the present status of the GEM project. In Sect. 3 we describe our portable single-dish scanning experiment at 2.3 GHz during three observing seasons in Colombia and Brazil. In Sect. 4 we outline the data reduction and preparation of a combined map with 69% of sky coverage between  $\delta = -51^{\circ}44'$  and  $\delta = +35^{\circ}37'$ . We discuss our results in the light of the Rhodes/HartRAO survey at 2326 MHz (Jonas et al. 1998) in Sect. 5 and, finally, we state our conclusions and future prospects in Sect. 6.

## 2. Radio continuum surveys and the GEM project

Unparalleled efforts have always been dedicated to delineate the complex morphology of the synchrotron-dominated Galactic emission at meter and centimeter wavelengths, which reveals the rich environment of supernova remnants with spurs and loops emanating from the Galactic Plane and, in some cases, engulfing our location near the inner Perseus spiral arm of the Galaxy. The work of Jansky and Reber led naturally to the completion of the first all-sky radio surveys. The earliest of these was the 200 MHz survey of Dröge and Priester (1956), which combined the observations of Allen and Gum (1950) in the Southern Hemisphere. The advent of the world's largest radiotelescopes, together with an improvement in the performance of the receivers, prompted the realization of several partial surveys of better sensitivity and resolution at 178 MHz (Turtle & Baldwin 1962), 30 MHz (Mathewson et al. 1965), 38 MHz (Milogradov-Turin & Smith 1973), 85 MHz and 150 MHz (Yates et al. 1967; Landecker & Wielebinski 1970), which were used to synthesize three additional low-frequency all-sky surveys: the 30 MHz map of Cane (1978), the 85 MHz map of Yates (1968) and the 150 MHz map of Landecker & Wielebinski (1970). The integrity of these maps is, however, compromised by the need to assume spectral indices when combining different frequencies and by significant sidelobe level corrections due to differential ground and sky pick-up; let alone the differences in the mapping strategy of each radiotelescope.

A major improvement in the preparation of all-sky surveys was achieved by Haslam et al. (1981; 1982), whose 408 MHz map of the whole sky reflects the choice of a single observing frequency and mapping strategy across four surveys to obtain a resolution under  $1^{\circ}$  with negligible sidelobe contamination. More recently another all-sky survey of similar characteristics was completed at 1420 MHz through the observations of Reich & Reich (1982; 1986) in the Northern Hemisphere and those of Testori et al. (2001) in the Southern Hemisphere (Reich et al. 2001). Ground based experiments to survey the radio continuum of the Galaxy have not been pursued at higher frequencies, with the exception of the Rhodes/HartRAO survey at 2326 MHz (Jonas et al. 1998) over 67% of the sky with a HPBW =  $0^{\circ}333$ ; whereas at lower frequencies three other major surveys have obtained 69% and 95% of total sky coverage at 22 MHz (Roger et al. 1999) and 45 MHz (Alvarez et al. 1997; Maeda et al. 1999).

In the last decade, the detection of temperature anisotropies in the Cosmic Microwave Background (CMB) radiation by the DMR experiment onboard the *COBE* satellite (Smoot et al. 1992) initiated a scientific breakthrough for cosmology; but it also showed, from the analysis of the *COBE* all-sky maps at 30 GHz, 53 GHz & 90 GHz (Bennett et al. 1992), the need to ex-

tend our knowledge of Galactic emission to higher frequencies. Since then, new generations of ground (e.g. BEAST – Childers et al. 2005; Meinhold et al. 2005; O'Dwyer et al. 2005), balloon (e.g. BOOMERanG – de Bernardis et al. 2000), and satellite experiments (WMAP – Bennett et al. 2003) have been and are being developed to measure the CMB with higher precision and resolution, to the level where polarisation measurements have become one of observational cosmology's hottest topics.

The success of high precision CMB observations, however, depends heavily on reliable and accurate separation of the cosmological signal from the foreground emission of our own Galaxy, which cannot be removed by any improvement in the detectors, whether on the ground or in space. Several techniques have become available; from simple Galaxy masking of heavily contaminated regions and point sources (e.g. Mejia et al. 2005) to the novel approaches of component separation and foreground removal (Hobson et al. 1998; Maino et al. 2002; Delabrouille et al. 2003; Eriksen et al. 2004; Bonaldi et al. 2006) which exploit the spectral and spatial diversity of the different astrophysical and cosmological components. Recently, the multi-frequency design of the *WMAP* mission revealed an impressive picture of unprecedented precision of the CMB at 23 GHz, 33 GHz, 41 GHz, 61 GHz and 94 GHz (Hinshaw et al. 2007).

### 2.1. The frequency gap

There is a considerable gap in our knowledge of large scale structure of Galactic emission between the upper frequency end of the large ground-based radiotelescopes and the lower end achievable from space or balloons, which confronts radioastronomers and cosmologists alike. Among the problems to be resolved from observations in this frequency gap is a better understanding of the variations in the synchrotron spectral index across the sky. The roll-off in the energy spectrum of relativistic electrons is expected to introduce breaks in the spectrum of the non-thermal component up to a few GHz, which can have significant impact in addressing the elusive nature of an anomalous dust-correlated Galactic component (Draine & Lazarian 1998; 1999); as well as in identifying spectral decrements in the black body curve of the CMB signal (Burigana et al. 1991; Bartlett & Stebbins 1991).

The lack of surveys in this frequency gap is even more critical for polarisation surveys. Synchrotron radiation is intrinsically polarised and its contaminating role poses higher risks for polarisation than for total intensity. In addition, the selection effect of Faraday depolarisation is partial only toward the lower end of the gap. It was not until recently though, that the first all-sky absolutely-calibrated polarisation survey (1.4 GHz) became a reality (Wolleben et al. 2006; Testori et al. 2004). Still, the gap extends up to the lowest of the *WMAP* frequency bands (Page et al. 2007). From the point of view of cosmological implications, it becomes more urgent to bridge radio and microwaves polarisation surveys; whereas from the astrophysical point of view, the precise elucidation of the Galaxy as a Faraday screen is of key importance to the study of magnetic fields in the Galaxy (Beck 2007) via the synchrotron mechanism. Clearly, polarisation surveys at frequencies higher than a few GHz (see for example Leonardi et al. 2006) are needed to address the contamination of the CMB at higher frequencies, where the forthcoming Planck mission, with a wider frequency coverage and a better sensitivity, will deepen our cosmological understanding.

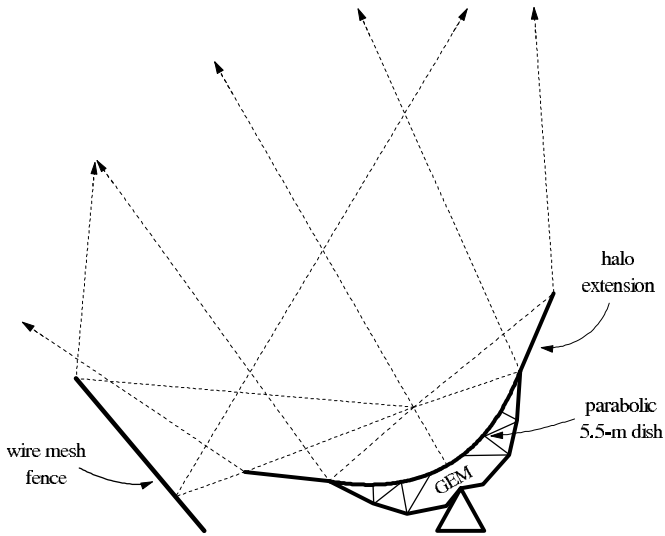


**Fig. 1.** A ray-tracing diagram (dotted lines) of the illumination properties of the double-shielded GEM dish. The rim-halo is 2.1 m long and the ground screen levels the horizon with a 10° high azimuth profile. Under full illumination, the dish subtends an angle of 158° at the prime focus.

## 2.2. The Galactic Emission Mapping project

The concept of the GEM project dates back to 1992 when the first detections of CMB anisotropies called for an improved understanding of Galactic emission (Smoot et al. 1992; Bennett et al. 1992) to eliminate foreground contamination from genuine cosmic signals. The existing radio continuum surveys suffered from two major shortcomings. First, they lacked mutual consistency in their baseline levels (Lawson et al. 1987; Banday & Wolfendale 1991) to be able to predict reliably the spectrum of Galactic synchrotron emission in the cosmologically interesting windows. Second, the spatial templates traced by the non-thermal component in the 408 MHz and 1420 MHz surveys were compromised by striping along the scanning direction of the radiotelescopes (Davies et al. 1996). Thus, the initial goal of the GEM project became the production of an atlas of total sky brightness maps at 408 MHz, 1465 MHz, 2.3 GHz, 5 GHz and 10 GHz, which would overcome these undesired radioastronomical shortcomings (De Amici et al. 1994; Smoot 1999). Improved mapping of the spectral and large scale properties of Galactic synchrotron radiation would also allow re-examination of baseline and destriping in former surveys.

At the core of the GEM project stood the development of a portable 5.5-m double-shielded radiotelescope, which could be deployed at different geographic latitudes to obtain uniform and consistent data sets. Since ground contamination is one of the most common sources of systematic errors in this type of survey experiments, the two shields were built to minimize sidelobe pick-up of stray radiation and to level out the horizon profile at the site location. These shields are schematically drawn in Fig. 1 and consisted, respectively, of: (a) a rim halo of aluminum panels extending tangentially from each of the 24 dish petals; and (b) a concentric network of inclined wire mesh ground screens. Tello et al. (1999; 2000) modelled their diffraction and attenuation properties to estimate the spillover and diffraction sidelobe contamination seen in elevation scans with the back-fire helical feeds at 408 MHz and 1465 MHz.

Diurnal and seasonal variations in the temperature of the ground also add low frequency noise to survey measure-

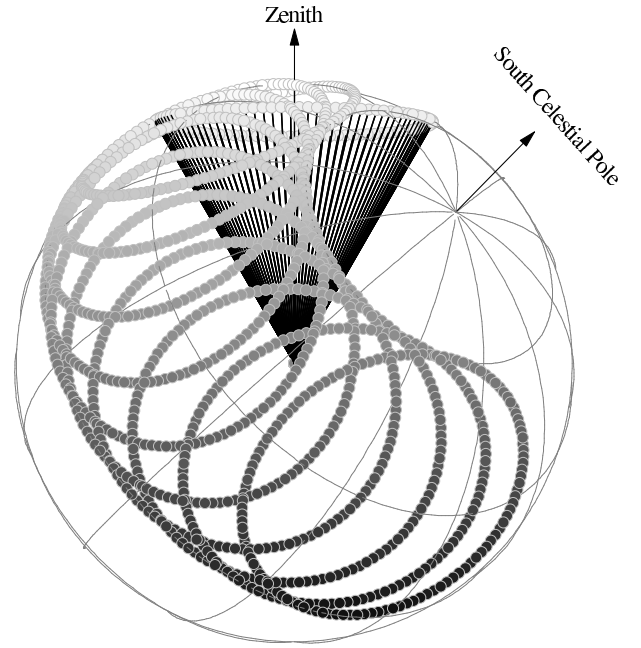


**Fig. 2.** Schematic representation of the mapping strategy of the GEM experiment for achieving sky coverage of a full declination band with half-width equal to the Zenith angle of the circular scans. In this figure,  $Z = 30^\circ$  scans have been spaced at 1-hour intervals for a site in the Southern Hemisphere.

ments carried out continuously over extended periods of time. Similarly, the variability of atmospheric emission introduces, in addition to low frequency noise, short term contributions in the scale of minutes. In order to make individual scans insensitive to atmospheric fluctuations, while still being able to map large areas of the sky, we adopted azimuthal scans of sufficiently high constant speed (1 rpm for  $Z = 30^\circ$  scans at 2.3 GHz). Coupled to the rotation of the Earth, these Zenith-centered circular scans achieve coverage of full declination bands with round-the-clock observations as shown schematically in Fig. 2.

Table 1 lists a summary of the main GEM observational campaigns since its first deployment in the Owens Valley desert near Bishop, CA, in 1993. In this period, the ground and rim-halo shields were continuously refurbished and upgraded to achieve satisfactory levels of ground rejection up to 10 GHz. A new rim-halo was re-designed and installed in 2001, whereas the ground screen has gone through two major upgrades to incorporate a finer mesh along with a more robust support structure (two ground shields have been lost due to unusually gusty and strong wind). Another great impediment for radio astronomical surveys is the ever increasing usage of the spectrum by human related activities, which plagues the radio environment with non-negligible levels of radio frequency interference (RFI). 100% duty-cycle interferers have aborted GEM operations several times in the past (the 408 MHz campaign in 1994, the 1465 MHz runs in 1995, and follow up observations at 2.3 GHz in 2004). In preparation for the GEM polarisation measurements at 5 GHz and 10 GHz, we have been conducting site surveys to avoid foreseeable RFI at these frequencies. The recent inclusion of Portugal in the GEM collaboration promises to deliver 5 GHz and 10 GHz polarisation templates of Stokes  $I$ ,  $Q$  and  $U$  parameters from both, the Southern and Northern, Hemispheres before the end of the present decade. The GEM-P program will certainly benefit from a carefully chosen site (Fonseca et al. 2006).

**Table 1.** Total intensity observations with the GEM experiment

Frequency	HPBW	Sky coverage	Duration	Site & Year	Reference
408 MHz	10°5	+07° < $\delta$ < +67°	40 h	Bishop, CA–USA 1994	Rodrigues 2000
1465 MHz	4°2	+07° < $\delta$ < +67°	70 h	Bishop, CA–USA 1994	Tello 1997
408 MHz	11°3	−24° < $\delta$ < +36°	447 h	Villa de Leyva – Colombia 1995	Torres et al. 1996
2.3 GHz	3°7	−24° < $\delta$ < +36°	231 h	Villa de Leyva – Colombia 1995	Torres et al., internal report
1465 MHz	4°2	−52° < $\delta$ < +08°	709 h	Cachoeira P., SP–Brazil 1999	Tello et al. 2005
2.3 GHz	2°3 × 1°8	−52° < $\delta$ < +08°	532 h	Cachoeira P., SP–Brazil 1999	Tello et al., this article
1465 MHz	4°2	−52° < $\delta$ < +08°	510 h	Cachoeira P., SP–Brazil 2004/2005	Tello et al., in preparation

### 3. The experiment at 2.3 GHz

The portability of the GEM experiment reduces its operation to three main modules: (a) a dish pedestal with an altazimuthal rotating platform; (b) a radiometer and (c) a control unit. These are graphically displayed in Fig. 3 with a slip rings assembly aligned with the axis of rotation along the base column of the dish pedestal. Their task is to distribute power to the scanning dish and to establish a communication protocol with the radiometer. Two interface boxes, one in the ground and another attached to the co-rotating base column, provide the connecting ports for the slip rings. A 1-hp AC-motor, controlled by frequency inverters and coupled to the main gear of the pedestal by means of a speed reducer, provided the motion in azimuth. An optical shaft encoder was afixed to the bottom of the slip rings assembly to measure the angular variations of the rotating platform. Similarly, an elevation encoder was installed on the dish horizontal axis. The analog signals of both encoders are also sent to connecting ports in their respective interface boxes, from where they are routed to the data acquisition box located on the elevation support arm beneath the dish. The data acquisition system (DAS) assembles the data frame by digitizing the analog inputs from the encoders, the radiometer and a noise source, before sending it seamlessly through the slip rings up to the control panel for storage on a PC.

#### 3.1. Data acquisition system

The data acquisition system (DAS) uses three single-width NIM modules to interface with the experiment and a data logging PC. The control module has an EPROM with a 16-channel data frame burnt in and an output connector for a serial output line. The analog multiplexer/ADC module receives 16 differential analog inputs of FSD  $\pm 10$  V with a common mode rejection of 86 dB. The ADC limits hard at  $\pm 10$  V with no bleed-over between channels and overloads of  $\pm 30$  V. In addition to the EOF signal, the DAS also times the firing of a thermally stable noise source every 80 frames. The noise source is kept underneath the dish surface inside an insulated box and transmits an  $\approx 140$  K reference signal from a small front-fire helix sitting along the junction of two of the dish petals. Two analog channels are dedicated to record the temperature and the voltage of the noise source. Finally, a serial-to-RS232 module takes the seamless serial data and synchronizes each frame with the hexadecimal EB90 word for decoding in the PC. LabView routines were used successfully with Macintosh and Pentium PC's to log the data. Proper time-stamping of the data followed by adding UT from a WWV digital receiver clock to the data frame for the observations in Colombia; whereas the WGS84 datum from a GPS receiver provided the time reference for the observations in Brazil.

#### 3.2. Radiometric characterization

For the observations at 2.3 GHz we used the three-legged support structure of the parabolic reflector to secure a direct-gain total-power radiometer at its focal plane by means of a latching mechanism. Its feed is built-in at the bottom of the radiometer enclosure, as shown in Fig. 4, and consists of a flanged cylindrical horn with  $1/4\text{-}\lambda$  chokes and a measured VSWR of 1.023 at 2.3 GHz (return loss of  $-39$  dB). Its circular aperture provides suitable illumination of the primary with a symmetric beam and a discrimination of  $-16$  dB at the edge of the reflector. Since the Moon is a reasonable approximation of a point source for our beam, horizontal and vertical beam patterns were obtained directly from the survey data by mapping the signal onto a Moon-centered coordinate system. With our circular scanning strategy, the horizontal pattern is derived from the antenna response when the Moon reaches the same elevation of the scanning circle; while the vertical pattern is established from the antenna response when the dish azimuth coincides with that of the Moon. These beam pattern profiles are shown in Fig. 5 for the data collected at the Colombian and Brazilian sites. Using gaussian fits to these profiles we obtained an average horizontal beam width of  $2^\circ.306 \pm 0^\circ.028$  and an average vertical beam width of  $1^\circ.848 \pm 0^\circ.098$  from the two experimental set-ups. Assuming that the secondary introduces no beam distortion, the 25% larger horizontal beam is an upper limit to the smearing of the beam due to the rotation of the antenna. Using internal errors only, this smearing of the mean is significant at the  $4.5\sigma$  level.

The power fed by the reflector is captured at the throat of the horn by a waveguide probe, which sends it down a section of semi-rigid coax into a front-end HEMT (High Electron Mobility Transistor) amplifier. As depicted in Fig. 3, the RF chain of the receiver section attains a nominal total amplification of  $\sim 70$  dB. The HEMT amplifier has a flat response across the entire 100 MHz width of the bandpass defining filter and a noise temperature of  $\approx 30$  K at an operating temperature of 300 K. After the filter, the signal is rectified by a square-law detector diode and its DC voltage is amplified by a factor of 500 (low gain) or 1000 (high gain). The DC amplifier is housed with a thermo-regulating circuit and a timing board inside a detached electronics box. The timing board subdivides the pulses from an end-of-data frame (EOF) signal generated in the data acquisition box in order to sample the DC voltage with a time constant of  $\tau = 0.56002$  s.

For the receiver to achieve an optimal performance, its gain variations were kept to a minimum by thermally stabilizing the interior of the RF-tight radiometer enclosure  $\approx 10^\circ\text{C}$  below the temperature set-point of the aluminum RF plate. To accomplish this functionality, we used a Peltier cooling unit on the side of the radiometer to continuously extract heat from its interior; while the thermo-regulating circuit maintained the RF plate (physical) temperature at its set-point by means of a sensing diode on the

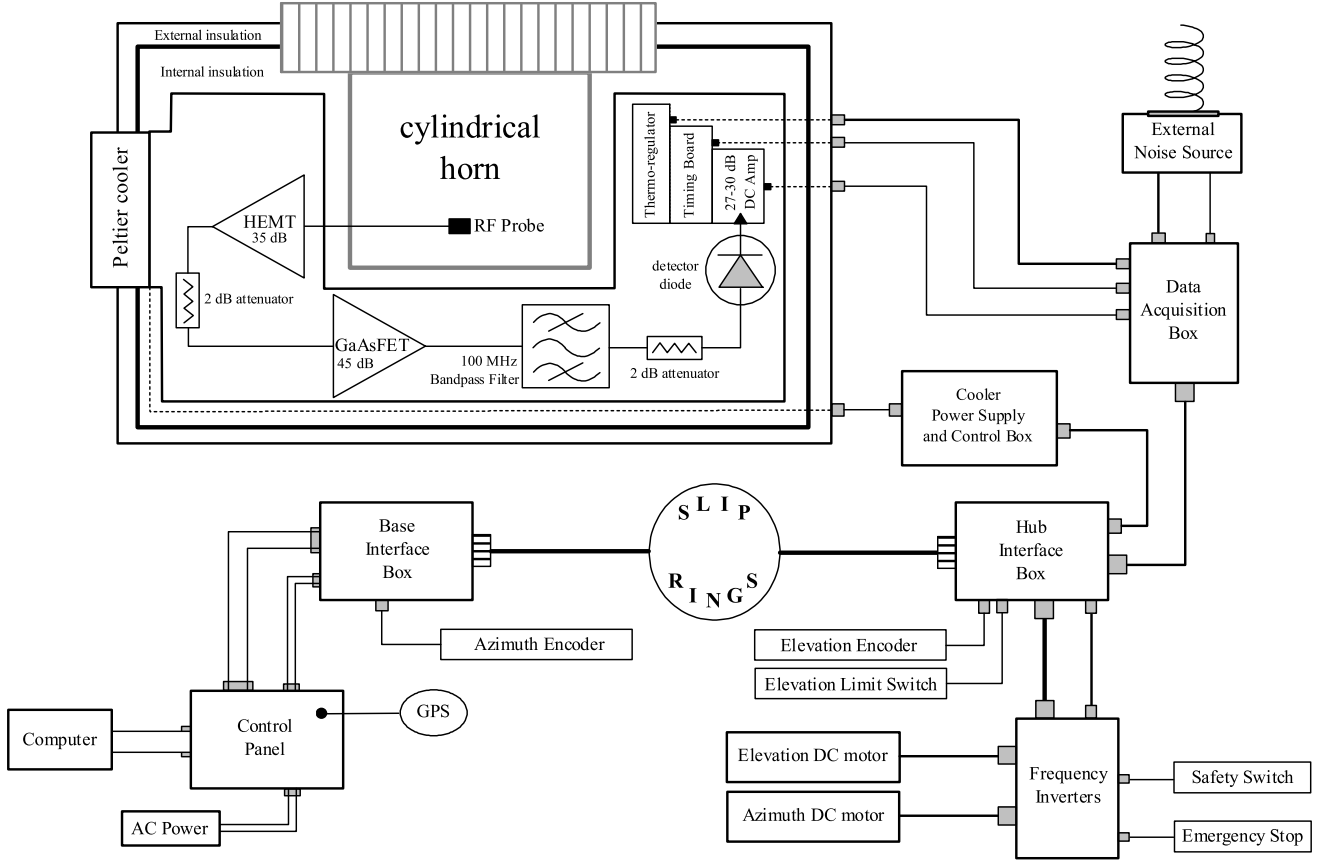


**Fig. 3.** Graphical layout of the GEM experiment at 2.3 GHz.

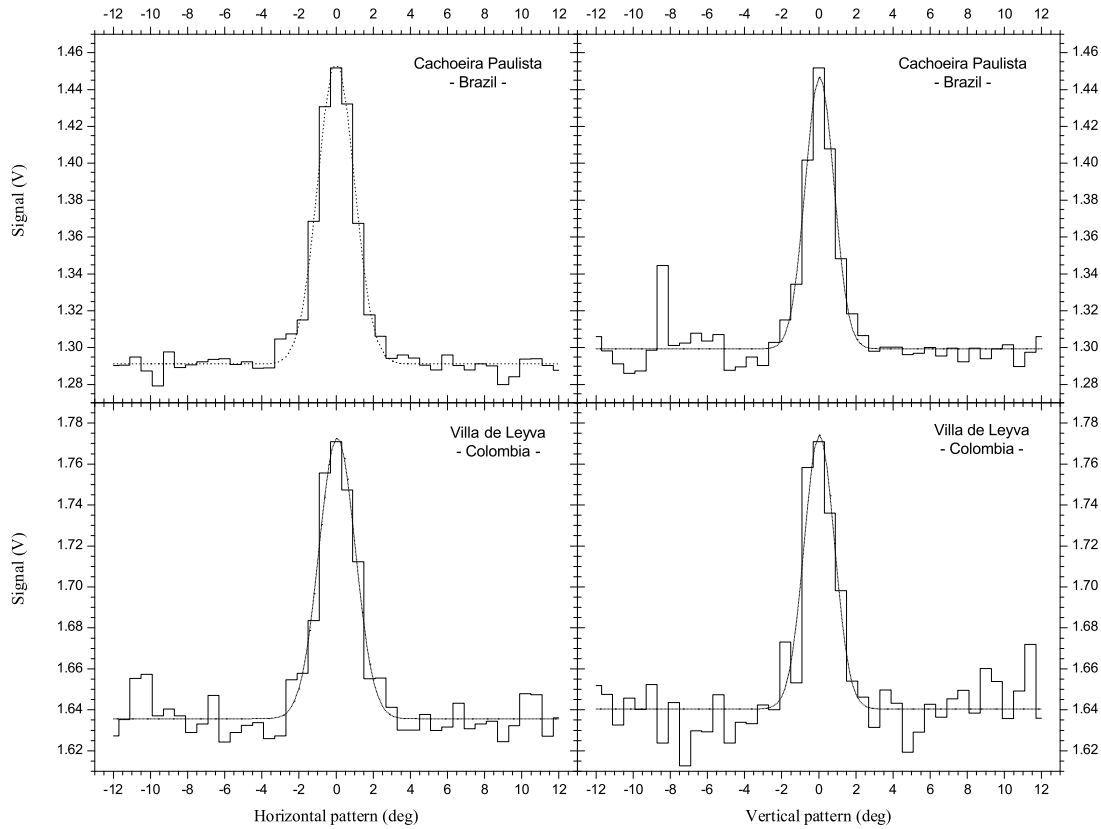


**Fig. 5.** Beam pattern characterization at 2.3 GHz from Moon measurements during routine survey scans away from the Galactic Plane. Gaussian fits to these profiles (dotted lines) were used to calibrate the antenna temperature scale of our maps.

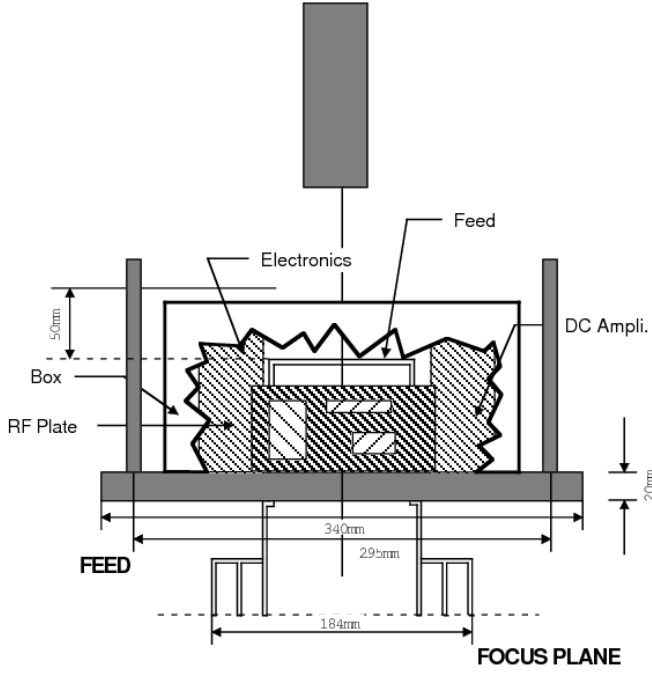


**Fig. 4.** Focal configuration at 2.3 GHz with a direct-gain total power radiometer.

plate to actively control a set of power resistors. The rest of the RF enclosure was coated internally and externally with insulating styrofoam. Four calibrated temperature sensors monitored constantly the thermal state of the radiometer at the detector diode, the HEMT amplifier, the horn flange and the electronics box.

The overall system performance was calibrated against the amplitude of the Moon signal shown in Fig. 5, which we compared to the expression of Krotikov & Pelyushenko (1987) for the brightness temperature at the center of the lunar disk at 2.3 GHz according to

$$T_{MB}^{\text{Moon}} = 221.63 + 3.14 \cos(\Omega t - 45^\circ), \quad (1)$$

where  $\Omega t$  denotes the dependance on the optical phase of the Moon and sets the Full Moon at  $\Omega t = 0$ . This expression is equivalent to the one obtained by Mangum (1993), except that the one above allows for the averaging action of the antenna beam pattern. A summary of calibration constants and antenna parameters obtained with this method is given in the second part of Table 2.

There are some disadvantages with this method which impact the accuracy of our estimates, but we have assessed the uncertainties in several ways to guarantee a reliable temperature scale for our map. Independent estimates of the total and main beam solid angles are the main source of uncertainty, since the ratio of the beam efficiency,  $\epsilon_M$ , and the aperture distribution factor,  $\kappa_p$ , which scales the product of the horizontal and vertical beam widths into the main beam solid angle, enter our gain calculation. Assuming a ratio of  $\epsilon_M/\kappa_p = 0.75/1.05$  we have tested the validity of the Moon calibration method by factoring out the total beam solid angle from its relation to the effective aperture, such that

$$S_{Jy} = \pi R_{\text{Moon}}^2 \frac{2k}{\lambda^2} \left( \frac{T_{MB}}{S_{\text{volts}}^{\text{peak}} - S_{\text{volts}}^{\text{ref}}} \right)_{\text{Moon}}$$

$$\times \left( \frac{S_{\text{volts}}^{\text{peak}}}{1 - \eta_G \Delta T_{\text{cal}}^{\text{peak}}} - \frac{S_{\text{volts}}^{\text{ref}}}{1 - \eta_G \Delta T_{\text{cal}}^{\text{ref}}} \right)_{\text{source}}, \quad (2)$$

where  $S_{Jy}$  is the flux density of an observed known source,  $R_{\text{Moon}}$  is the radius of the lunar disk,  $S_{\text{volts}}$  is the signal output of the radiometer in volts,  $\eta_G$  is the thermal gain susceptibility in Table 2 and  $\Delta T_{\text{cal}}$  is the temperature drift of the RF plate from its mean temperature during the Moon  $S_{\text{volts}}^{\text{peak}}$  measurements. We chose Vir A and Cen A to test the calibrating Moon amplitude in the Colombian and Brazilian data sets, respectively. Vir A is sufficiently smaller than our beam size and we obtained 134 fu using eq. 2 compared to 140 fu using Baars et al. (1977) semi-absolute spectrum between 400 MHz and 25 GHz as given by

$$\log S_{\text{VirA}}[\text{fu}] = 5.023(\pm 0.034) - 0.856(\pm 0.010) \log \nu_{\text{MHz}}. \quad (3)$$

The Baars scale was updated by Ott et al. (1994) to assess source variability and they obtained new measurements at  $\lambda = 21, 11, 6$  and 2.8 cm for Vir A, which allowed them to fit a second order polynomial between 1408 MHz and 10.55 GHz, such that

$$\log S_{\text{VirA}}^{\text{Ott}}[\text{fu}] = 4.484 - 0.603 \log \nu_{\text{MHz}} - 0.028 \log^2 \nu_{\text{MHz}}. \quad (4)$$

However, at our frequency of 2.3 GHz this revised scale produces 138 fu, which does not differ significantly from the Baars scale. Cen A, on the other hand, is an extended source covering some  $4^\circ \times 10^\circ$  in celestial coordinates, so we targeted its brightest component, the North-East inner lobe, and obtained 94 fu compared to 99 fu using Alvarez et al. (2000) integrated flux density relation between 80 MHz and 43 GHz as given by

$$\log S_{\text{CenA}}[\text{fu}] = 4.35(\pm 0.08) - 0.70(\pm 0.02) \log \nu_{\text{MHz}}. \quad (5)$$

The less than 5% discrepancy between our estimates of both sources and the published values lends substantial support to the use of the observed amplitude of the Moon signal to calibrate our antenna temperature scale. The ratio  $\epsilon_M/\kappa_p$  does not enter eq. 2 explicitly, but it is implied in the calculation of the RF plate physical temperature drift. Given the good agreement between observed and published fluxes, the assumed ratio restrains the beam efficiency to the range defined by the uncertainty quoted in Table 2 on behalf of the expected range for  $\kappa_p$  alone ( $1.00 \leq \kappa_p \leq 1.05$ ).

An additional source of uncertainty with the Moon calibration method is the need to estimate the temperature of the reference background level above which the Moon signal is superimposed. This level consists of two isotropic components, the CMB radiation and a small contribution of the diffuse background of extragalactic emission, but it also includes Galactic foreground radiation, atmospheric emission and stray radiation from the ground through the sidelobes. The isotropic components are well known,  $2.725 \pm 0.002$  K for the CMB (Mather et al. 1999) and 0.027 K for the extragalactic background (Lawson et al. 1987). Likewise, we estimated the atmospheric emission at  $1.64 \pm 0.07$  K for the Colombian site and at  $2.29 \pm 0.13$  K for the Brazilian site according to the modeling prescription of Danese & Partridge (1989). As for the Galactic foreground component, the observations of the Moon took place in regions away from the Galactic Plane, so that an estimate of  $0.8 \pm 0.4$  K was used in agreement with successive refinements of the calibration constants during the removal of the stray radiation component. The assessment of ground contamination proved to be the single most challenging aspect in the preparation of the GEM 2.3 GHz map, as will be seen in the next section, and for this reason the system temperature estimate given in Table 2 includes the contribution of the ground.

**Table 2.** GEM 2.3 GHz survey

Colombia		Brazil
Villa de Leyva −73° 35′ 0.53″ +5° 37′ 7.84″ 2173 Jun 1–18 (1995)	Geographical Name Longitude Latitude Altitude (m.a.s.l.) Observing runs	Cachoeira Paulista −44° 59′ 54.34″ −22° 41′ 0.74″ 572 May 18 – June 17 October 11–26 (1999)
altazimuthal 1 rpm 46.3% 2300 MHz 100 MHz 54.675 K V <sup>−1</sup> −0.02381 ±0.00028 85.466 K 11.42 mK 310.572 K 2:30 ± 0:13 1:92 ± 0:18 75 ± 3.5% 29.9% 306 Jy K <sup>−1</sup>	antenna mounting azimuth scanning speed sky coverage (Z = 30°) Centre frequency Pre-detection bandwidth Gain Gain susceptibility (K <sup>−1</sup> ) System Temperature RMS sensitivity RF plate T <sub>cal</sub> horizontal HPBW vertical HPBW beam efficiency aperture efficiency Point source sensitivity	altazimuthal 1 rpm 46.8% 2300 MHz 100 MHz 50.928 K V <sup>−1</sup> −0.02164 ±0.00006 61.644 K 8.24 mK 308.031 K 2:31 ± 0:03 1:82 ± 0:12 75 ± 3.5% 31.4% 290 Jy K <sup>−1</sup>

#### 4. Data description and processing

The data used in the preparation of the GEM 2.3 GHz map was collected during three observational seasons at the Colombian and Brazilian sites listed in Table 1. A brief description of each observational site and their associated data sets is given in the first part of Table 2. We used  $Z = 30^\circ$  scans for a total combined sky coverage of  $\approx 66\%$ . In Fig. 6 we have summarized the major steps in the preparation of the combined map.

##### 4.1. Time stamping and pointing calibration

The Colombian data set had each frame tagged with UT seconds and we adjusted a simple linear progression with a step size of  $\tau$  seconds to time stamp each frame. For the Brazilian data, we relied on an iterative process to minimize the difference between the timing of the frames in the time line of 1-s updates of the GPS receiver and the expected cadence of the seamless data stream. We broke the latter into equal time slots of 2<sup>h</sup> and 34<sup>m</sup> to facilitate detection and correction of systematics during the data collection. Smaller time slots were inevitable whenever interruptions of the scanning process were encountered in lining up the TOD or the data stream was found to be corrupted.

Readings from the azimuth angle encoder were first scaled to match 360° rotations of constant speed and then the Ephemeris of the Sun was used to estimate the offset between the astronomical azimuth of the Sun and the encoder readout for the peak of the radiometer signal during scans that brought the GEM circle in the sky close to the Sun. In order to guarantee a consistent mechanical configuration for all the scans, we used a calibrated steel bar to lock the dish into pre-defined elevation angles. Fine tuning of the actual azimuth and elevation angles was accomplished by centering the Moon image in a Moon-centered coordinate system as shown in Fig. 7.

**Table 3.** Low Galactic emission regions

Colombia survey		
Col 1	141°0 ≤ RA <sub>2000</sub> ≤ 146°0	30°0 ≤ DEC <sub>2000</sub> ≤ 35°0
Col 2	134°5 ≤ RA <sub>2000</sub> ≤ 139°5	28°5 ≤ DEC <sub>2000</sub> ≤ 33°5
Col 3	136°0 ≤ RA <sub>2000</sub> ≤ 141°0	1°5 ≤ DEC <sub>2000</sub> ≤ 6°5
Brazil survey		
Br 1	45°0 ≤ RA <sub>2000</sub> ≤ 50°0	−33°0 ≤ DEC <sub>2000</sub> ≤ −28°0
Br 2	54°0 ≤ RA <sub>2000</sub> ≤ 59°0	−33°0 ≤ DEC <sub>2000</sub> ≤ −28°0
Br 3	37°0 ≤ RA <sub>2000</sub> ≤ 42°0	−30°0 ≤ DEC <sub>2000</sub> ≤ −25°0

##### 4.2. Total power systematics

Once the time ordered data were properly synchronized, we extracted the raw signal of the Moon and we proceeded to calibrate the radiometer constants as described in Sect. 3.2. Of these constants, the thermal gain susceptibility,  $\eta_G$ , required extraction of the raw signal observed in pre-defined regions of low Galactic emission, or cold sky regions as evidenced in the 408 MHz survey of Haslam et al. (1982), in order to monitor the linear response of the radiometer signal output as a function of the RF plate physical temperature. Fortuitively, these low emission regions were scanned during routine day-time hours, when the drift in  $\Delta T_{\text{cal}}$  displayed its largest excursions and, thus, enabled accurate linear fits to the signal-RF plate temperature correlation. A set of three regions of  $5^\circ \times 5^\circ$  were chosen for each site as listed in Table 3 and the linear correlation coefficients of each set were averaged and scaled by the corresponding ratio of Gain to system temperature to obtain  $\eta_G$ .

Total power systematics are both linear and non-linear in nature. Thermal gain susceptibility corrections address some of the systematics of the linear type. Non-linear gain variations, on the other hand, cannot be corrected without additional time-series analysis of the data stream. Initially, we had intended to use the periodical firings of the noise source to correct gain variations in general. However, after some careful analysis of the noise source amplitude variations, we found that the noise source had become unstable in the course of time and that its use as a transfer calibrator failed to meet the accuracy we required. In order to filter odd-behaved data, we turned to an alternate criterion, which relied on the distribution of the minimum observed antenna temperature,  $T_A^{\text{min}}$ , per time slot (154<sup>m</sup> max). Non-linear excursions of the baseline were found to correspond to low values of  $T_A^{\text{min}}$ , so we fixed lower limits for its distribution to improve the characterization of the systematics affecting the survey.

For this purpose we split the Brazilian survey into 3 separate data sets, comprising each about 2 weeks of data collection, and whose characteristics reflect the seasonality effect between summer and winter, but also the long term performance of the experiment over a month of winter observations. The first of the two Brazilian winter data sets coincided with the same period of the year as the single Colombian data set. Fig. 8 shows the distribution of  $T_A^{\text{min}}$  for the four data sets. All three Brazilian data sets are seen to be well contained under a single-peaked distribution centered around 4.5 K, whereas the Colombia data are not as smoothly distributed with a main peak below 3 K, a secondary peak coinciding with the single peak of the Brazilian data sets and a likely third and smaller peak around 6 K. Although a realistic lower limit at 3.5 K could be chosen for the Brazilian data, a value of 2 K had to be used for the Colombian data set in order to avoid excessive dissipation of the survey.

The clumpy distribution of  $T_A^{\text{min}}$  in the Colombian data set does have an immediate effect in the mapping of its survey data

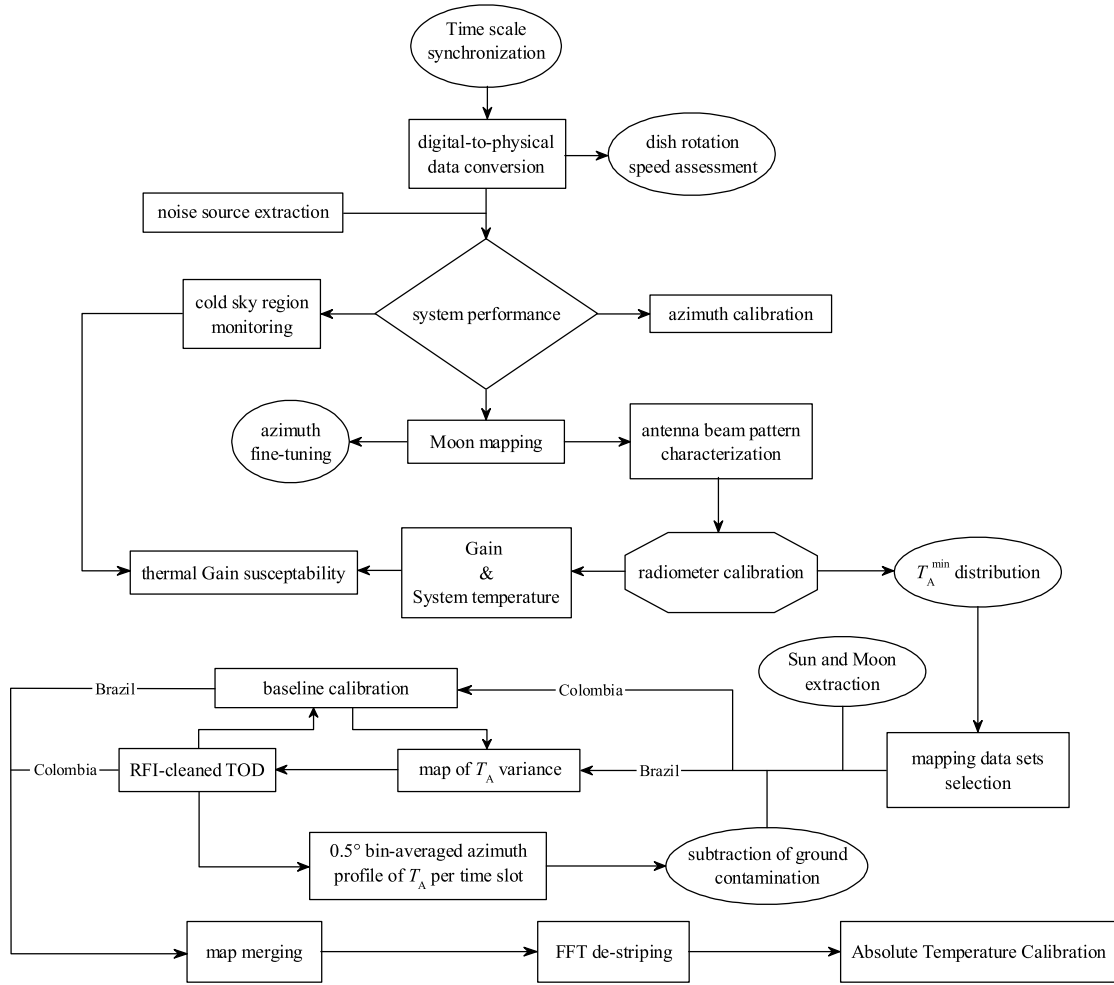


**Fig. 6.** Overview of the survey data processing.

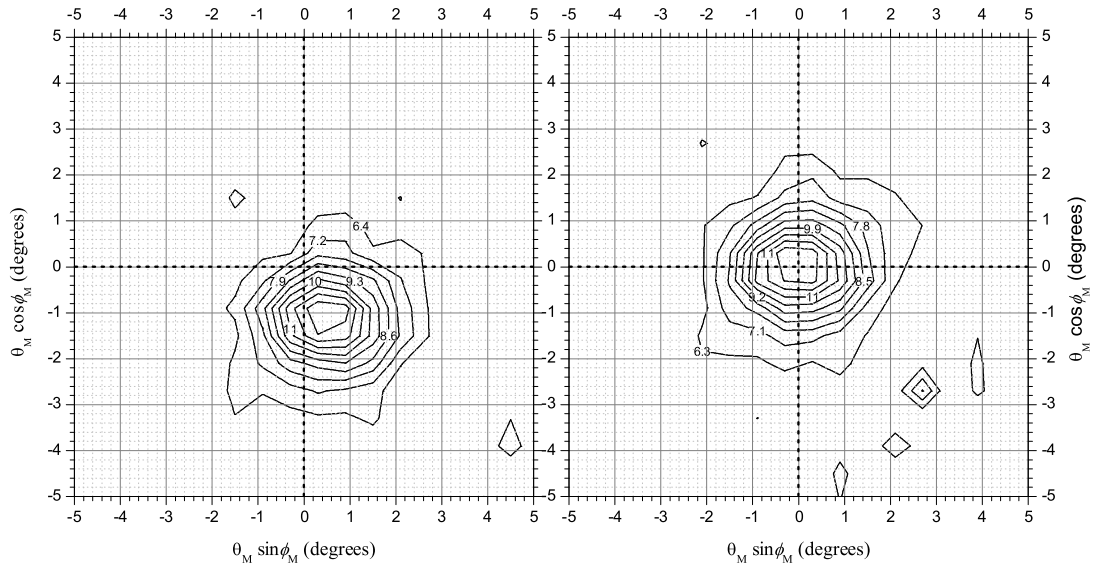


**Fig. 7.** Fine tuning of the pointing calibration constants was achieved by allowing the mapping of the Moon to be centered at the Ephemeris-specified position of the Moon. The maps in this figure re-project the polar coordinates,  $\theta$  and  $\phi$ , of the boresight onto a celestial grid centered on the Moon.



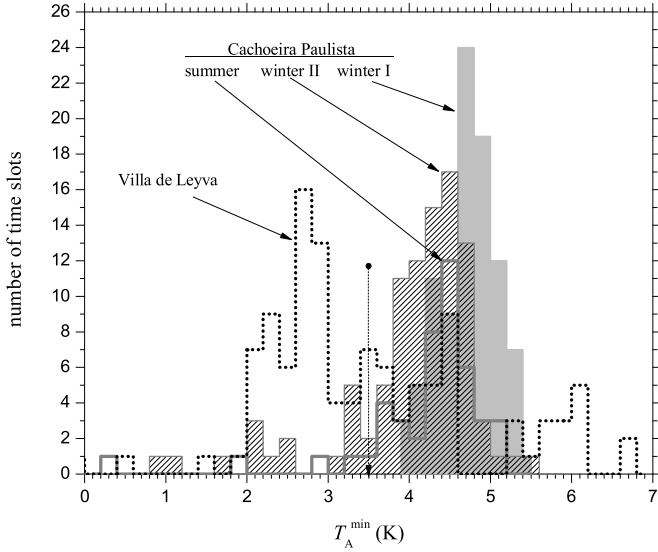


**Fig. 8.** Distribution of the minimum observed antenna temperature in data collected from Colombian and Brazilian data sets. The arrow indicates the limiting threshold for the Brazilian sets.

as can be seen in Fig. 9, which shows clear evidence of an inhomogeneous baseline as scan-induced circular striping. On the other hand, mapping of the Brazilian survey shows a smoother baseline contrast, but a rather different and disturbing systematic shows up in the form of heavy striping in declination as a result of substantial ground pick-up in the Northern part of the Cachoeira Paulista sky.

#### 4.3. RFI and ground contamination removal

Both maps in Fig. 9 show several bright spots due to man-made interference (RFI), whose excision was accomplished by means of a low-pass filter during a 4-step iteration process aimed to remove the ground striping. In the Colombia map there is also the sinusoidal streak left by an artificial satellite, whose transmissions highlight portions of the contaminating track. To remove this type of RFI, a tedious monitoring of the survey time slots was conducted and the affected time slots were deprived of observations found within the perimeter of the satellite streak.

The cleaning of the ground striping proved, on the other hand, to be an homogeneous baseline-dependant process and it was applied iteratively to the Colombian and Brazilian data sets in slightly different ways as indicated at the bottom of Fig. 6. For both data sets, the process started by flagging the presence of the Sun and Moon whenever their angular separation from the observing direction was less than  $30^\circ \rightarrow 60^\circ$  and  $6^\circ$ , respectively. Subsequently, a variance map of the antenna temperatures in the remainder of the survey was obtained; except that the inhomogeneous baseline of the Colombian data set required its baseline to be calibrated as described in Sect. 5 before its variance map was obtained. In a second step, the observations were compared to the variance map on a per pixel basis and a new set of TOD was assembled from those observations which did not exceed 3 times the variance in the corresponding pixel. A pixel resolution of  $360/256^\circ = 1.40625^\circ$  was chosen in order to prevent undersampling for the size of our data sets. In the third iteration step, the new and RFI-cleaned TOD were averaged in azimuth to produce mean profiles of the ground contamination for each observed time slot, as long as the observations were distanced

**Table 4.** Surveyed data composition.

Description	Colombia		Brazil	
	Duration	(%)	Duration	(%)
Total survey time	162 <sup>h</sup> 85	100.00	532 <sup>h</sup> 11	100.00
Corrupted data	4 <sup>h</sup> 13	2.54	–	–
TOD mismatch	6 <sup>h</sup> 56	4.03	–	–
Noise source firings	11 <sup>h</sup> 41	7.01	39 <sup>h</sup> 91	7.5
Sun and Moon	17 <sup>h</sup> 0	10.44	78 <sup>h</sup> 11	14.68
$T_A^{\min}$ exclusion	4 <sup>h</sup> 38	2.69	43 <sup>h</sup> 36	8.15
RFI	2 <sup>h</sup> 46	1.51	3 <sup>h</sup> 46	0.65
Total mapping time	116 <sup>h</sup> 91	71.79	367 <sup>h</sup> 27	69.02

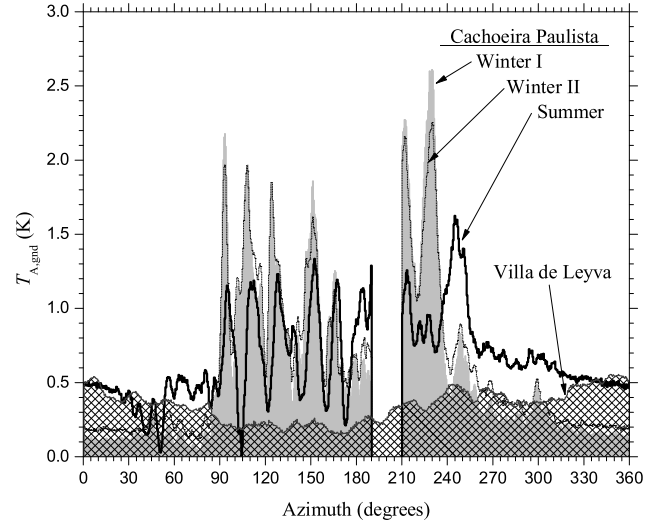


**Fig. 10.** Cumulative overall-mean azimuth profiles of the ground contamination component of the antenna temperature.

more than  $30^\circ$  from the Galactic Plane to prevent real sky features to appear as contaminating signatures in the mean azimuth profile. Finally, in the last and fourth step, an overall mean azimuth profile for each of the 4 data sets was secured by excluding any remaining isolated sky feature. This was accomplished with a low-pass filter, which looped over the azimuth profiles from all the time slots in a given set, to exclude profile points with more than 3 times the variance per azimuth bin ( $0.5^\circ$  wide). The loop was repeated until no more profile points were excluded. From here on, the 4-step iteration process was repeated, except that the subtraction of the normalized overall-mean azimuth profile from the previous iteration was subtracted in the first two steps. The normalization consisted in offsetting the profile down by the amplitude of its lowest profile point. In this way, the ground contamination was successively eliminated until the overall-mean azimuth profile of the last iteration was practically reduced to zero.

Fig. 10 shows the cumulative overall-mean azimuth profiles of the four data sets after meeting the convergence criterion. The spiky Brazilian profiles reflect the nature of the striping in declination, but they also bring forth the seasonality effect and the need to assess winter and summer data sets separately. As expected, the profile of the Colombian data set shows the contamination from the ground to be much lower and less variable. Still, residual horizontal striping remained visible in the final iterated map and additional destriping was applied in the final preparation of the map as described in the next section.

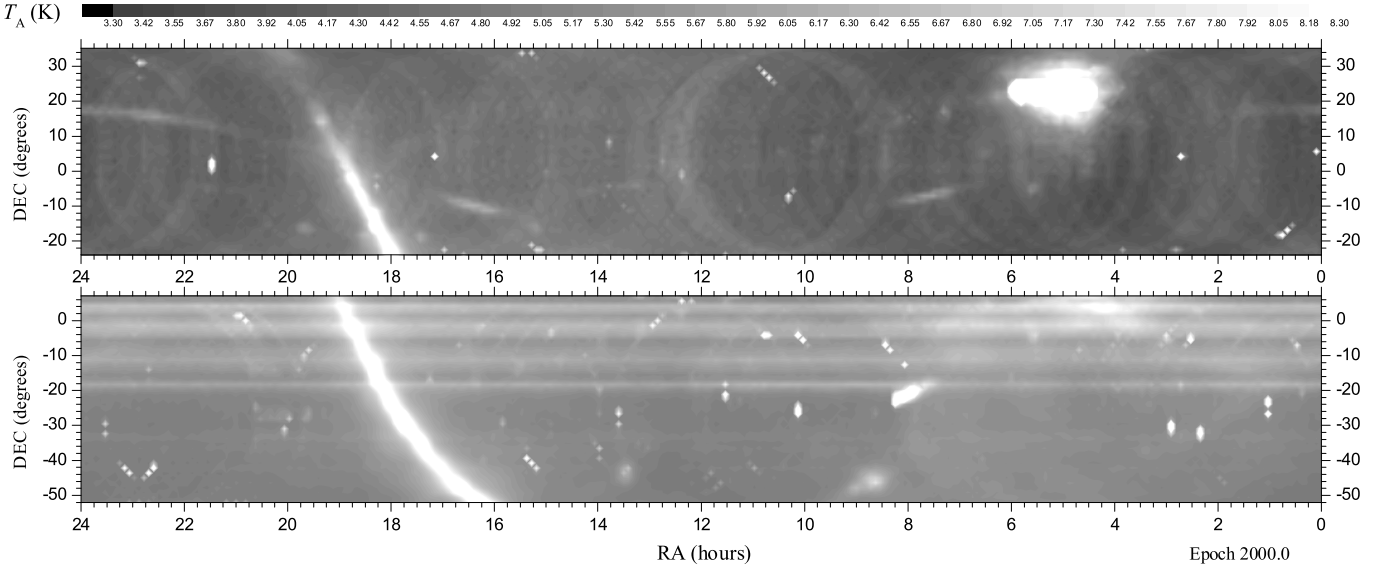


**Fig. 9.** Maps of unprocessed survey data from selected time slots ( $T_A^{\min}$  limited) in the Colombia and Brazil's first winter data sets. The Sun is the prominent feature around 5<sup>h</sup> of RA in the Colombia map

Table 4 summarizes all the cuts applied to the data sets as a result of the selection and cleaning processes described so far. A more conservative minimum angular separation of  $60^\circ$  for the Sun was used with the Brazilian data sets to eliminate traces of scattering sidelobes from the three-legged feed support structure as well as to guarantee a safer margin of secondary sidelobe suppression. The angular separation for the Colombian data set at  $30^\circ$  reflects the lack of conclusive evidence for sidelobe contamination at larger angular separations due to the reduced sensitivity from a smaller data volume. Corrupted data and TOD mismatch did not apply to the Brazilian data sets, since an automatic data collection algorithm was implemented to keep the observational time slots of equal length.

## 5. Final map preparation and calibration

The final preparation of the GEM 2.3 GHz survey was divided in three major steps. First, the baseline of the ground-subtracted Brazilian data sets was calibrated and the resulting map was merged with the one from the cleaned Colombian data set. Second, the destriping technique developed by Platania et al. (2003) was applied to the merged map to clean residual striping due to ground contamination and baseline inhomogeneities. Third, a direct comparison with the Rhodes/HartRAO survey at 2326 MHz (Jonas et al. 1998) was performed to absolutely calibrate the GEM survey.

### 5.1. Baseline calibration

In order to reduce the circular stripes introduced by the scanning technique in the TOD of the Brazilian data set, its baseline was calibrated following the same prescription that was applied to the Colombian data set (see Fig. 6). This calibration consisted in resolving the true sky temperature distribution at the level where its coldest contour would intersect, at least once, every survey scan (a  $60^\circ$  wide circular scan centered at the Zenith with a  $2:30 \times 1:85$  HPBW). In other words, the coldest observation of every survey scan would be normalized to a uniform temperature, or apparent zero-point of our temperature scale, across the entire declination band. This assumption is, to a first order ap-

proximation, sufficient to correct the  $1/f$ -noise in the TOD as the dominant source of baseline inhomogeneity, but it also defines an effective full-beam brightness temperature scale for the survey.

When applied to the Colombian data set, the precision of the baseline calibration was set by the level of the fluctuations in the ground profile of Fig. 10, or  $62 \pm 16$  mK. Without this *a priori* calibration, the ground profile fluctuations would have increased to  $1357 \pm 424$  mK and they would have compromised any subsequent baseline calibration. For comparison, the ground profile fluctuations in the Brazilian data averaged to  $355 \pm 55$  mK in the Winter I,  $350 \pm 56$  mK in the Winter II and  $362 \pm 57$  mK in the Summer data set before their baseline was calibrated. This difference in implementing the baseline calibration did not allow the Colombian and Brazilian surveys to be merged along their entire region of overlap ( $-23^\circ \lesssim \delta \lesssim +6^\circ$ ). Instead, an offset of  $148 \pm 24$  K was applied to the Colombian data according to the difference between the two surveys along the Northern boundary (best signal-to-noise ratio) of the Brazilian survey for  $\alpha \lesssim 17$  h and around an overlapping rectangular region  $\sim 11^\circ$  wide for  $\alpha \gtrsim 17$  h. The merging of the two surveys in this overlap region allowed reciliant traces of ground striping in the Brazilian survey to be reduced. Ultimately, the baseline calibration relied on the uniformity in the sampling of the surveyed sky area. With our observational technique of Zenith-centered circular scans, the sky is sampled preferentially towards the edges of the declination band. This intrinsic bias diminishes with the number of observations by statistical virtue alone and, thus, contributed to the baseline differences between the two maps. Of course, cuts in the TOD, such as those indicated in Table 4, also affected the sampling uniformity and introduced additional baseline inhomogeneities.

### 5.2. Cleaning of residual striping

The merged map showed traces of residual striping, whose RMS level could be estimated at 58 mK after filtering the zero-frequency component of the map in Fourier space. The FFT destriping technique of Platania et al. (2003) was subsequently applied to produce a cleaner map. The technique was adapted from

**Table 5.** Distribution of percentage temperature variations  $\delta T$  in destriped pixels of the 2.3 GHz GEM and 2326 MHz Rhodes/HartRAO surveys.

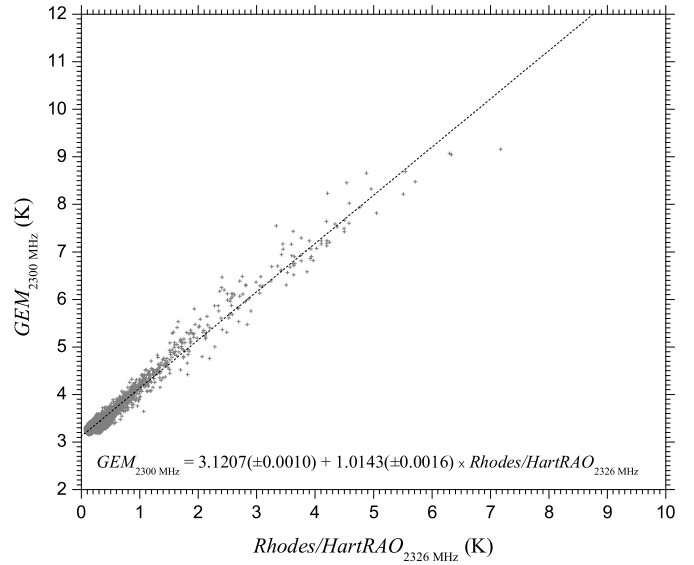
survey	$\delta T$ (%) interval			
	< 1	(1,5)	(5,10)	> 10
GEM ( $\Delta T < 0$ K)	6.5%	22.1%	13.9%	6.0%
GEM ( $\Delta T > 0$ K)	5.9%	17.2%	12.0%	16.4%
GEM	12.4%	39.3%	25.9%	22.4%
Rhodes/HartRAO	18.3%	50.6%	22.5%	8.6%

a method applied by Schlegel et al. (1998) to destripe the IRAS map and uses source extraction and stripe identification thresholds in 30 partially overlapping patches of  $32 \times 32$  pixels for the GEM map. This small number of pixels per patch and the corresponding large angular dimension was suitable to address the variability of the striping pattern in the merged map and resulted in the stripe image shown in Fig. 11 with a RMS level of 22 mK. The procedure was not applied to 5 patches (15.1% of the map) containing the Galactic Plane due to large signal gradients and a clean GEM map was obtained by subtracting the stripe image from the merged map.

The destriping procedure was applied in Platania et al. (2003) to the 408 MHz full-sky map of Haslam et al. (1982) and to the 1420 MHz (Reich 1982, Reich & Reich 1986) and 2326 MHz (Jonas et al. 1998) surveys. Given the importance of the latter for the absolute calibration of the GEM map, we compare in Table 5 the effect of the destriping on the GEM and Rhodes maps in terms of the percentage temperature variations  $\delta T$  of the pixels. Nearly half of the destriped pixels in the GEM map did not exceed variations of more than 5%, whereas in the Rhodes map the corresponding percentage of pixels was higher ( $\approx 70\%$ ). Still, we have examined the significance of the variations larger than 5% for the GEM map and Table 5 also shows the distribution of the percentage variations in two temperature regimes; one of positive residuals ( $\Delta T > 0$  K) and another of negative residuals ( $\Delta T < 0$  K). Despite the large contribution of pixels with  $\Delta T > 10$  K, the average positive residual was only  $27 \pm 17$  mK in this range; whereas the smaller fraction of pixels with  $\Delta T < 10$  K averaged into a significantly larger negative residual of  $-51 \pm 44$  mK. For variations in the  $5\% < \delta T \leq 10\%$  range, the average residuals were  $13 \pm 11$  mK and  $-18 \pm 13$  mK. Altogether, the destriping resulted in a small excess of negative residuals, which implies that the ground subtraction slightly over-corrected this type of contamination.

### 5.3. Absolute calibration

The absolute calibration of the baseline was obtained by means of a  $T$ - $T$  plot between destriped versions of the GEM and Rhodes maps. The Rhodes survey, from which the isotropic components of the CMB and the diffuse extragalactic background had been subtracted, was convolved with a Gaussian profile having a FWHM of  $140'$  to match the GEM survey. The overlap between the two surveys covers the declination range  $-51^\circ \lesssim \delta \lesssim +30^\circ$  after excluding boundary systematics. Using a celestial grid with a resolution of  $360/256^\circ = 1.40625^\circ$  produced 13 132 paired pixels, whose  $T$ - $T$  plot is shown in Fig. 12 along with a linear fit (98% correlation) for calibrating the true zero-point of the GEM survey baseline. Notwithstanding the spectral implications due to the small deviation of the linear coefficient from unity ( $+14.3 \pm 1.6$  mK  $K^{-1}$  is equivalent to a temperature ratio between

**Fig. 12.**  $T$ - $T$  plot between the destriped GEM survey at 2300 MHz and the Rhodes/HartRAO survey at 2326 MHz.

two synchrotron components, had the GEM band been centered at  $2314.05 \pm 0.45$  MHz), we can alternatively estimate the zero-point correction from the straight mean of the pixel-by-pixel temperature differences at  $3.125 \pm 0.092$  K. Similarly, the distribution of these pixel differences is nearly normal as shown in Fig. 13 with a Gaussian envelope centered at  $3.1356 \pm 0.0019$  K and standard deviation of  $65.5 \pm 1.9$  mK. An important feature of the destriping procedure is that it has negligible effect on the temperature scale of the map and, to illustrate this, we have included in Fig. 13 the Gaussian envelope and its underlying distribution of pixel differences for the ground-corrected map before the destriping. We estimate the error in the zero-level of our survey at 103 mK by combining in quadrature the standard deviation of the pixel differences with the error of 80 mK in the absolute zero-level of the Rhodes survey, according to their calibration with the absolute sky temperature measurements of Bersanelli et al. (1994) at 2 GHz from the South Pole. Our estimate agrees with the expected accuracy of the Moon-calibrated temperature scale in Sect. 3.2, where we quoted an error  $< 5\%$  which the cold sky baseline calibration translates into  $< 156$  mK. Similarly, the difference between the apparent, Moon calibration-dependant, zero-point and its true value is 108 mK.

The clean and calibrated GEM survey at 2.3 GHz is presented in Fig. 14. It is a template of the synchrotron-dominated radio continuum of our Galaxy together with a familiar host of bright Galactic and extragalactic sources. Its brightness temperature scale is tied up to both, the resolution limited approach of the cold sky baseline calibration and the full-beam definition of the Rhodes survey. We can obtain a conversion factor between the full beam estimates of the two surveys by correlating linearly the GEM survey with the unconvolved version of the Rhodes survey. This gives a conversion factor  $0.8151 \pm 0.0031$ , which checks reasonably well against 0.8641 for the emission ratio in the direction of the Galactic Center, given the 5% uncertainty of the Rhodes temperature scale and the compounded error in the zero-level accuracy of the GEM survey.

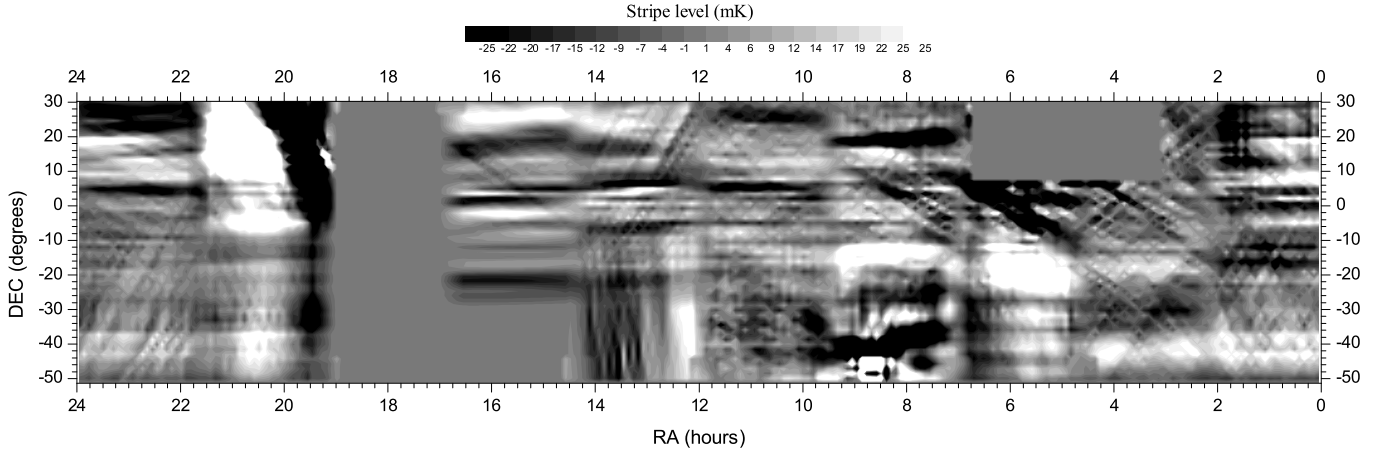


**Fig. 11.** Map of residual stripping obtained with the FFT filtering technique of Platania et al. (2003) on the ground-corrected merged map.

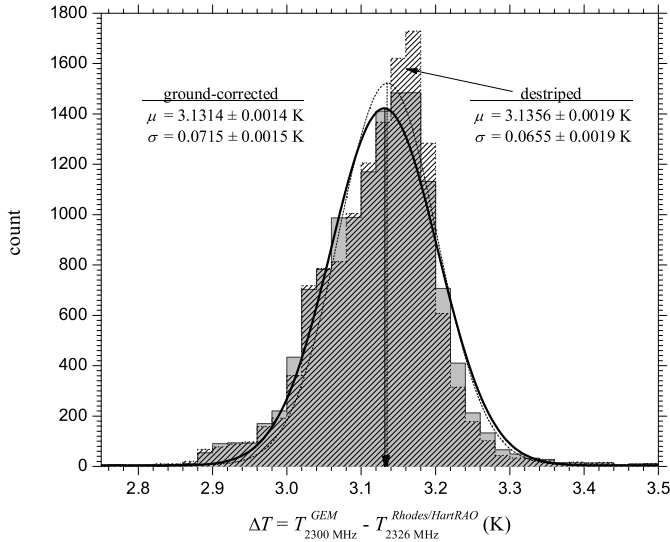


**Fig. 13.** Distribution of pixel-by-pixel temperature differences between GEM and Rhodes maps before (ground-corrected) and after the destriping.

## 6. Conclusions and future prospects

The preparation of low frequency surveys from the ground poses considerable challenge to scientific endeavours, given the need to combine the stability of instrument performance with observational constraints over long periods of time. Any mismatch in this process introduces systematic effects, which radioastronomers aim to keep under control by designing experiments that can address the desired balance between the proposed science and enduring logistics. The GEM project has evolved in this scenario for over a decade with the ultimate goal to improve our understanding of Galactic synchrotron emission in total intensity and polarisation between 408 MHz and 10 GHz, signaling the ever-increasing impact that foreground contamination has for the CMB community.

In this article we present our efforts at 2.3 GHz by combining observations obtained with a portable 5.5-m radiotelescope in Colombia and Brazil to produce a synchrotron template of Galactic emission with 69% sky coverage from  $\delta = -53^\circ$  to  $\delta = +35^\circ$  with a HPBW of  $2:30 \times 1:85$ . The main focus of our

analysis has been a thorough assessment of the systematics that affected the observations; in particular, the ground contamination.

The results presented in this article summarize one of the main phases in the developing of the GEM project, which started with the total intensity 408 MHz survey of Torres et al. (1996) and is currently dedicated to polarisation measurements of the Galactic foreground at 5 GHz. With observations at 5 GHz already into the second year of observations from the Brazilian site, we are scheduling the release of the first GEM polarisation survey for 2008. Combined with the 5 GHz polarization survey of our Portuguese collaborators, we hope to provide the CMB community with substantial feedback to improve the study cases of milestone experiments like the Planck satellite mission and future CMB polarisation experiments. Plans to engage our efforts into a follow-up polarisation experiment at 10 GHz will most likely begin to take shape in the near future, while the preparation of spectral index maps between the four working frequencies of the project (408 MHz, 1465 MHz, 2.3 GHz and 5 GHz) promises yet to reveal an astrophysically interesting scenario for increasing our knowledge and understanding of the nature and composition of the synchrotron component of the Galactic emission.

**Acknowledgements.** We are enormously grateful to several generations of students and technicians at LBNL and INPE, for whom GEM was an enriching learning experience. We are particularly in debt to John Gibson, Alexandre M.R. Alves, Luiz Arantes and Luiz Antonio Reitano for their skillful competence and inspiring performance. We also thank Jon Aymon, Tony Banday, Justin Jonas and Andrew Jaffe for helpful advice and SLB/INPE for logistics support in Cachoeira Paulista. The destriped version of the Rhodes/HartRAO map has been courtesy of Tony Banday. The GEM project in Brazil was supported by FAPESP through grants 97/03861-2, 97/06794-4 and 00/06770-2. T.V. acknowledges support from CNPq through grant 305219/2004-9. M.B. acknowledges the support of the NATO Collaborative Grant CRG960175. S.T. acknowledges the support provided by Colciencias funding of the GEM project in Colombia through project 2228-05-103-96, contract No. 221-96. D.B. acknowledges support from FCT – Portugal and POCI through an SFRH/BPD grant and project grants POCTI/FNU/42263/2001 and POCI/CTE-AST/57209/2004. The HealPix package was used to generate the Mollweide projection of the GEM survey.

## References

- Allen C. W. & Gum C. S. 1950, *Austr. J. Sci. Res.* A3, 224
- Alvarez H., Aparici J., May J. & Olmos F., 1997, *A&AS* 124, 315
- Alvarez H., Aparici J., May J. & Reich P., 2000, *A&A* 355, 863
- Baars J. W. M., Genzel R., Pauliny-Toth I. I. K. & Witzel A., 1977, *A&A* 61, 99
- Banday A.J. & Wolfendale A.W. 1991, *MNRAS* 248, 705

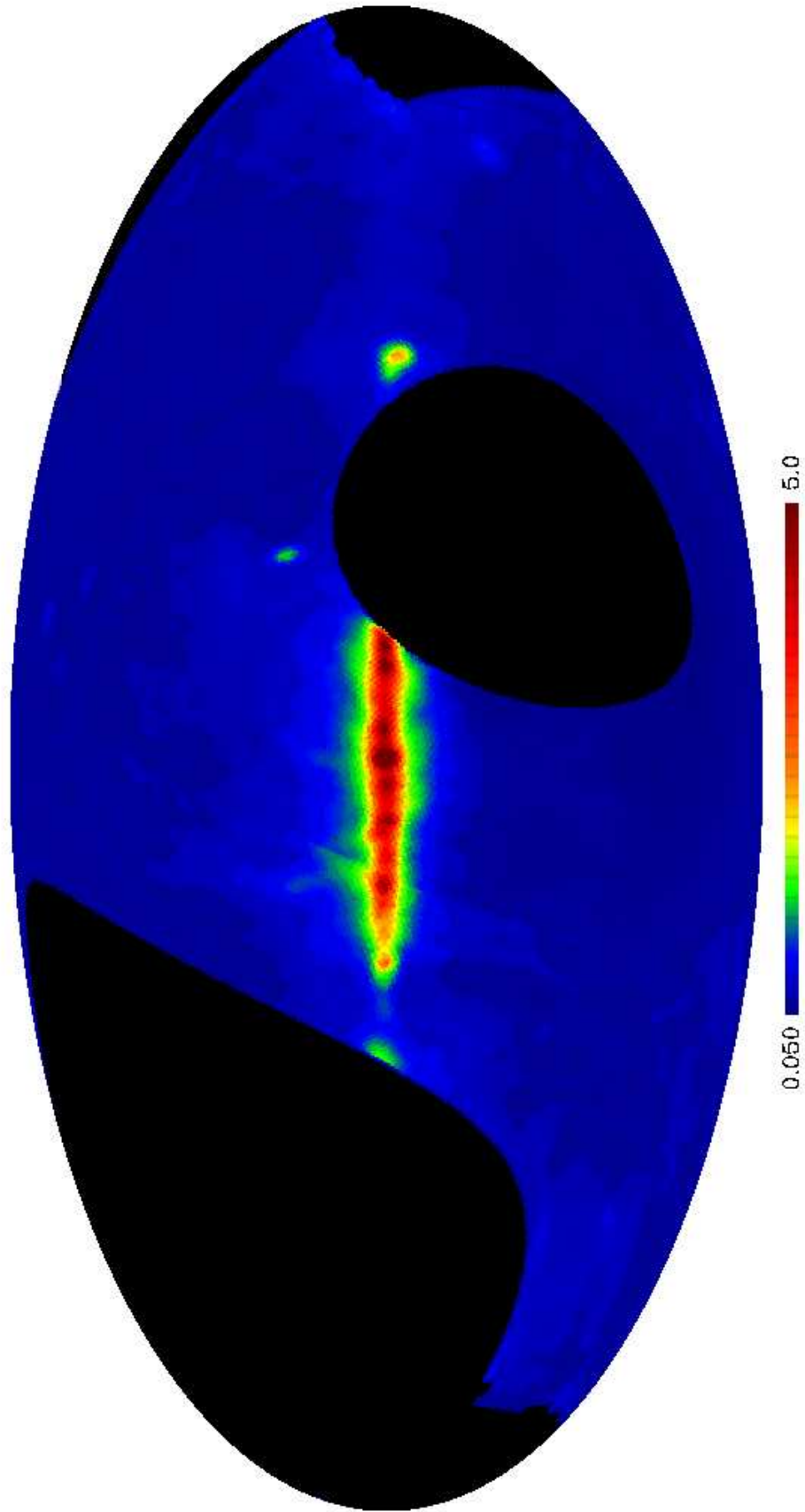


**Fig. 14.** Mollweide projection in Galactic coordinates of the structure of the radio continuum in the 2.3 GHz GEM survey.

- Bartlett J. G. & Stebbins A. 1991 *ApJ* 371, 8
- Beck R. 2007, in *EAS Publications Series 23, Sky Polarisation at Far-Infrared to Radio Wavelengths: The Galactic Screen before the Cosmic Microwave Background*, ed. M.-A. Miville-Deschênes and F. Boulanger, 19
- Bennett C. L., Hill R. S., Hinshaw G., et al. 2003, *ApJS* 148, 97
- Bennett C. L., Smoot G. F., Hinshaw G., et al. 1992, *ApJ* 396, L7
- Berkhuijsen E. M. 1972, *A&AS* 5, 263
- Bersanelli M., Bensadoun M., De Amici G., et al. 1994, *ApJ* 424, 517
- Bonaldi A., Bedini L., Salerno E., et al. 2006, *MNRAS* 373, 271
- Burigana C., Danese L. & De Zotti, G. F. 1991 *A&A* 246, 49
- Cane H. V. 1978, *Austr. J. Phys.* 31, 561
- Childers J., Bersanelli M., Figueiredo N., et al. 2005, *ApJS* 158, 124
- Danese L. & Partridge R. B. 1989, *ApJ* 342, 604
- Davies R. D., Watson R. A. & Gutiérrez C. M. 1996, *MNRAS* 278, 925
- De Amici G., Torres S., Bensadoun M., et al. 1994, *Ap&SS* 214, 151
- de Bernardis P., Ade P. A. R., Bock J. J., et al. 2000, *Nature* 404, 955
- Delabrouille J., Cardoso J.-F. & Patanchon G. 2003, *MNRAS* 346, 1089
- Draine B. T. & Lazarian A. 1998, *ApJ* 494, L19
- Draine B. T. & Lazarian A. 1999, *ApJ* 512, 740
- Dröge F. & Priester W. 1956, *ZAp* 40, 236
- Eriksen H. K., Banday A. J., Górski K. M. & Lilje P. B. 2004, *ApJ* 612, 633
- Fonseca R., Barbosa D., Cupido L., et al. 2006, *New A* 11, 551
- Haslam C. G. T., Klein U., Salter C. J., et al. 1981, *A&AS* 100, 209
- Haslam C. G. T., Salter C. J., Stoffel H. & Wilson W. E. 1982, *A&AS* 47, 1
- Hinshaw G., Nolte M. R., Bennett C. L., et al. 2007, *ApJS* 170, 288
- Hobson M. P., Jones A. W., Lasenby A. N. & Bouchet F. R. 1998, *MNRAS* 300, 1
- Jansky K. G. 1932, *Proc. I. R. E.* 20, 1920
- Jansky K. G. 1933, *Proc. I. R. E.* 21, 1387
- Jansky K. G. 1935, *Proc. I. R. E.* 23, 1157
- Jonas J. L., Baart E. E. & Nicolson, G. D. 1998, *MNRAS* 297, 977
- Kiepenhauer K. O. 1950, *Phys. Rev. A* 79, 738
- Krotikov V. D. & Pelyushenko S. A. 1987, *Soviet Ast.* 31(2), 216
- Landecker T. L. & Wielebinsky R. 1970, *Austr. J. Phys. Suppl.* 16, 1
- Lawson K. D., Mayer C. J., Osborne J. L. & Parkinson M. L. 1987, *MNRAS* 225, 307
- Leonardi R., Williams B., Bersanelli M., et al. 2006, *New Astronomy Reviews* 50, 977
- Maeda K., Alvarez H., Aparici J., et al. 2000, *A&AS* 140, 145
- Mangum J. G. 1993, *PASP* 105, 117
- Mather J. C., Fixsen D. J., Shafer R. A., et al. 1999, *ApJ* 512, 511
- Maino D., Farusi A., Baccigalupi C., et al. 2002, *MNRAS* 334, 53
- Meinhold P. R., Bersanelli M., Childers J., et al. 2005, *ApJS* 158, 101
- Mathewson D. S., Broten N. W. & Cole D. J. 1965, *Austr. J. Phys.* 18, 665
- Mayer C. H., McCullough T. P. & Sloanaker R. M. 1957, *ApJ* 126, 468
- Mejia J., Bersanelli M., Burigana C., et al. 2005, *ApJS* 158, 109
- Mills B. Y. 1959, *PASP* 71, 267
- Milogradov-Turin J. & Smith F. G. 1973, *MNRAS* 161, 269
- O'Dwyer I., Bersanelli M., Childers J., et al. 2005, *ApJS* 158, 93
- Ott M., Witzel A., Quirrenbach A., et al. 1994, *A&A* 284, 331
- Page L., Hinshaw G., Komatsu E., et al. 2007, *ApJS* 170, 335
- Platania P., Burigana C., Maino D., et al. 2003, *A&A* 410, 847
- Reber G. 1940, *Proc. I. R. E.* 28, 68
- Reber G. 1944, *ApJ* 100, 279
- Reber G. 1948, *Proc. I. R. E.* 36, 1215
- Reich W. 1982, *A&AS* 48, 219
- Reich P. & Reich W. 1986, *A&AS* 63, 205
- Reich P., Testori J. C. & Reich W. 2001, *A&A* 376, 861
- Rodrigues R. 2000, *MSc Thesis, Instituto Nacional de Pesquisas Espaciais, Brasil*
- Roger R. S., Costain C. H., Landecker T. L., et al. 1999, *A&AS* 137, 7
- Schlegel D. J., Finkbeiner D. P. & Davis M. 1998, *ApJ* 500, 525
- Smoot G. F., Bennett C. L., Kogut A., et al. 1992, *ApJ* 396, L1
- Smoot G. F. 1999, in *ASP Conf. Ser. 181, Microwave Foregrounds*, ed. A. de Oliveira-Costa and M. Tegmark, 61
- Tello C. 1997, *PhD Thesis, Instituto Nacional de Pesquisas Espaciais, Brazil*
- Tello C., Villela T., Wuensche C. A., et al. 1999, *Rad. Sci.* 34(3), 575
- Tello C., Villela T., Smoot G. F., et al. 2000, *A&AS* 145, 495
- Tello C., Villela T., Smoot G. F., et al. 2005, in *ASP Conf. Ser. 201, New cosmological data and the values of the fundamental parameters*, ed. A. Lasenby and A. Wilkinson, 138
- Testori J. C., Reich P. & Bava J. A., et al. 2001, *A&A* 368, 1123
- Testori J. C., Reich P. & Reich W. 2004, in *The Magnetized Interstellar Medium*, ed. B. Uyaniker, W. Reich and R. Wielebinski, 57
- Torres S., Cañon V., Casas R., et al. 1996, *Ap&SS* 240, 225
- Turtle A. J. & Baldwin J. E. 1962, *MNRAS* 124, 459
- Westerhout G., Seeder C. L., Brouw W. N. & Tinbergen J. 1962, *Bull. Astron. Inst. Netherlands* 16, 187
- Wielebinski R., Shakeshaft J. R. & Pauliny-Toth I. I. K. 1962, *Observatory* 82, 158
- Wolleben M., Landecker T. L., Reich W. & Wielebinski R. 2006, *A&A* 448, 411
- Yates K. W., Wielebinsky R. & Landecker T. L. 1967, *Austr. J. Phys.* 20, 595
- Yates K. W. 1968, *Austr. J. Phys.* 21, 167